J. Fluid Mech. (1997), *vol.* 347, *pp.* 263–287. Printed in the United Kingdom

© 1997 Cambridge University Press

Fully developed intermittent flow in a curved tube

By YUTAKA KOMAI† AND KAZUO TANISHITA

Institute of Biomedical Engineering, Faculty of Science and Technology, Keio University, 3-14-1 Hiyoshi, Kohokuku, Yokohama 223, Japan.

(Received 24 May 1995 and in revised form 31 January 1997)

Fully developed intermittent flow in a strongly curved tube was numerically simulated using a numerical scheme based on the SIMPLER method. Physiological pulsatile flow in the aorta was simulated as intermittent flow, with a waveform consisting of a pulse-like systolic flow period followed by a stationary diastolic period. Numerical simulations were carried out for the following conditions: Dean number $\kappa = 393$, frequency parameter $\alpha = 4$–27, curvature ratio $\delta = 1/2$, $1/3$ and $1/7$, and intermittency parameter $\eta = 0$–$1/2$, where η is the ratio of a systolic time to the cycle period. For $\alpha = 18$ and 27 the axial-flow profile in a systolic period becomes close to that of a sinusoidally oscillatory flow. At the end of the systole, a region of reversed axial velocity appears in the vicinity of the tube wall, which is caused by the blocking of the flow, similar to blocked flow in a straight tube. This area is enlarged near the inner wall of the bend by the curvature effect. Circumferential flow accelerated in a systole streams into the inner corner and collides at the symmetry line, which creates a jet-like secondary flow towards the outer wall. The region of reversed axial velocity is extended to the tube centre by the secondary flow. The development of the flow continues during the diastolic period for α higher than 8, and the flow does not completely dissipate, so that a residual secondary vortex persists until the next systole. Accordingly, the development of secondary flow in the following systolic phase is strongly affected by the residual vortex at the end of the previous diastolic phase, especially by stationary diastolic periods. Therefore, intermittent flow in a curved tube is strongly affected by the stationary diastolic period. For $\eta = 0$ and $1/5$, the induced secondary flow in a systole forms additional vortices near the inner wall, whereas for $\eta = 1/3$ and $1/2$ additional vortices do not appear. The characteristics of intermittent flow in a curved tube are also strongly affected by the length of the diastolic period, which represents a period of zero flow.

1. Introduction

The studies of unsteady flow in curved tubes initiated by Lyne (1970) have attracted interest not only for engineering applications to heat exchangers and chemical reactors, but also because of its relevance to hemodynamical problems (Pedley 1980). Pathological studies indicated that curved portions of arterial vessels are one of the favoured sites for atherosclerotic formation (Wesolowski *et al.* 1965), and these findings suggested that blood flow in the arterial vessel may play a major role in the localization of atherosclerosis (Gessner 1973). The blood flow in an aortic arch can

† Present address: Kawachi Millibioflight Project, JRDC. 5-9-1 Tokodai Tsukuba, Ibaraki 300-26, Japan.

https://doi.org/10.1017/S0022112097006538 Published online by Cambridge University Press

Authors	Waveform Averaged Dean number	Method Curvature ratio	Peak Dean number Frequency parameter
Smith (1975)	Pulsatile	Theoretical	high and small
	—	small	high and small
Lin & Tarbell (1980)	Pulsatile	Experimental (Numerical)	~ 600 (~ 200)
	~ 300 (~ 100)	1/5.4, 1/20	2.5–5.4(0–10)
Rabadi *et al.* (1980)	Pulsatile	Numerical	24–588
	$12 \sim 294$	1/100	4.8–24.7
Chandran & Yearwood (1981)	Physiological	Experimental	1140
	320	1/10	20.76
Talbot & Gong (1983)	Pulsatile	Experimental	372, 80.0
	58.8, 372	1/20, 1/7	8.0, 12.5
Chang & Tarbell (1985)	Pulsatile, Physiological	Numerical	163–1740
	120 594	$1/20 \sim 1/3.8$	$7 \sim 20.96$
Chang & Tarbell (1988)	Physiological	Numerical	$95.7 \sim 634.5$
	$49.5 \sim 382.9$	1/10	3.07–4.86
Hamakiotes & Berger (1988)	Pulsatile	Numerical	0.378–378
	$0.757 \sim 757$	1/7	15
Naruse *et al.* (1990*b*)	Pulsatile	Experimental	364.5, 599
	168, 291	1/3, 1/7	12.6, 18.1
Rindt *et al.* (1991)	Pulsatile	Numerical	327, 122
	204, 0	1/6	1–15
Konno *et al.* (1994)	Intermittent	Experimental	395.5
	—	1/3	13.8

TABLE 1. Summary of published work. 'Physiological' means measured blood waveform and 'pulsatile' is a sinusoidal waveform with a mean flow equal to the physiological mean flow.

be characterized by a high degree of pulsatility and curvature. Both pulsatility and curvature cause extremely complex time-dependent, three-dimensional flow patterns.

A number of theoretical and experimental studies on periodically unsteady flow in curved tubes have been carried out. Smith (1975) theoretically investigated the nature of pulsatile flow, which varied sinusoidally with a non-zero mean, in a gently curved tube (i.e. curvature ratio $\delta \ll 1$, where δ is the ratio of the tube radius to the curvature radius), and showed the presence of secondary streaming flow at both small and large frequency parameters, in spite of relatively low secondary Reynolds numbers of about unity. Lin & Tarbell (1980) studied pulsatile flow with moderate frequency parameters, and suggested the existence of a resonance between the secondary and axial flow, which is a striking feature of the pulsatility in a curved tube. The resonance phenomenon was verified by the highly peaked friction factor at intermediate frequencies, and the resonance frequency can be quantitatively predicted with theoretical models.

The blood flow in a curved artery is characterized as developing flow. Talbot & Gong (1983) measured pulsatile entrance flow in a curved tube by laser Doppler velocimetry (LDV) and found that at a frequency parameter $\alpha = 12.5$ ($\alpha = a(\omega/\nu)^{1/2}$, where a, ν and ω are the radius of the tube, the kinematic viscosity of the fluid, and the angular frequency of pulsation in a systole, respectively), separation of the axial flow appears at the inner bend near the downstream end during deceleration, and propagates upstream toward the pipe entrance. Rindt *et al.* (1991) calculated the velocity profile in the entrance flow for steady, oscillatory, and pulsatile flow

https://doi.org/10.1017/S0022112097006538 Published online by Cambridge University Press

conditions. They showed that steady secondary flow is caused by the steady component of the flow and appears at $\alpha = 24.7$. Furthermore, from their calculations using a pulse-like physiological waveform of $\alpha = 4.0$, they concluded that the diastolic phase has little effect on the flow occurring during the systolic phase.

However, the aortic flow waveform is characterized by intermittent flow rather than by sinusoidal flow (i.e. the flow waveform in the aorta consists of pulse-like systolic flow followed by the stationary diastolic period). Because intermittent flow in a curved tube has more physiological implications, Chandran & Yearwood (1981) measured three-dimensional flow distributions for conditions of intermittent flow. Furthermore, the strong curvature of an aortic arch (i.e. $\delta \approx 1/3$) considerably influences the oscillation of the wall shear stress profile (Naruse *et al.* 1990*b*). Therefore the blood flow in an aortic arch can be simulated as intermittent flow in a strongly curved tube, and δ becomes an independent parameter that governs the flow in a curved tube (Berger & Talbot 1983). The experimental studies of intermittent flow in a curved tube by Konno, Satoh & Tanishita (1994) showed that secondary flow is augmented in the diastolic stationary period. The numerical results of Chang & Tarbell (1985) exhibited complex secondary flows with up to seven vortices in the half-cross-section and cascaded vortex structures. However, the nature of intermittent flow is still not fully understood, and in particular, the effect of stationary diastolic periods on the flow variation in entire periods remains unknown.

The purpose of the present study, therefore, is to clarify the nature of intermittent flow in strongly curved tubes through numerical simulations, which simulate the physiological flow in the aortic arch.

2. Mathematical formulation

2.1. *Governing equations*

The toroidal coordinate system (figure 1) is used to describe periodically unsteady flow in a curved tube. We assumed that the fluid is incompressible and Newtonian, and the physical properties were considered constant in both space and time. Furthermore, the flow field was assumed to be axial fully developed, which implies that

$$\frac{\partial}{\partial \theta}(u, v, w) = 0. \tag{1}$$

Using (1) to represent the flow as fully developed, the final form of the momentum and continuity equations in conservation form can be written as follows:

$$\begin{aligned}
&\frac{\alpha^2}{Re}\frac{\partial u}{\partial t} + \frac{1}{rA}\left[\frac{\partial}{\partial r}(rAu^2) + \frac{\partial}{\partial \phi}(Auv) - Av^2 - \delta r\cos\phi w^2\right] \\
&\quad = -\frac{\partial p}{\partial r} + \frac{1}{Re}\left\{\frac{1}{rA}\left[\frac{\partial}{\partial r}\left(rA\frac{\partial u}{\partial r}\right) + \frac{\partial}{\partial \phi}\left(\frac{A}{r}\frac{\partial u}{\partial \phi}\right)\right]\right. \\
&\qquad \left. -\frac{1}{r^2}\left(2\frac{\partial v}{\partial \phi} + u\right) + \frac{v\delta\sin\phi}{rA} + \frac{\delta^2\cos\phi}{A^2}(v\sin\phi - u\cos\phi)\right\}, \qquad (2) \\
&\frac{\alpha^2}{Re}\frac{\partial v}{\partial t} + \frac{1}{rA}\left[\frac{\partial}{\partial r}(rAuv) + \frac{\partial}{\partial \phi}(Av^2) + Auv + \delta r\sin\phi w^2\right] \\
&\quad = -\frac{1}{r}\frac{\partial p}{\partial \phi} + \frac{1}{Re}\left\{\frac{1}{rA}\left[\frac{\partial}{\partial r}\left(rA\frac{\partial v}{\partial r}\right) + \frac{\partial}{\partial \phi}\left(\frac{A}{r}\frac{\partial v}{\partial \phi}\right)\right]\right. \\
&\qquad \left. +\frac{1}{r^2}\left(2\frac{\partial u}{\partial \phi} - v\right) - \frac{u\delta\sin\phi}{rA} - \frac{\delta^2\sin\phi}{A^2}(v\sin\phi - u\cos\phi)\right\}, \qquad (3)
\end{aligned}$$

https://doi.org/10.1017/S0022112097006538 Published online by Cambridge University Press

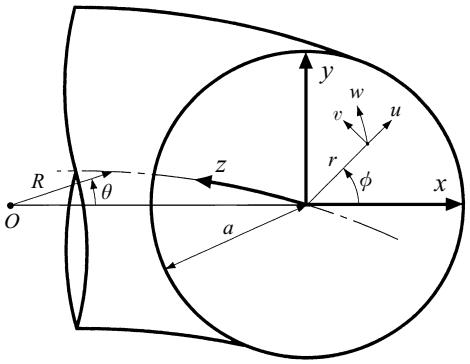


FIGURE 1. Toroidal coordinate system.

$$\frac{\alpha^2}{Re}\frac{\partial w}{\partial t} + \frac{1}{rA}\left[\frac{\partial}{\partial r}(rAuw) + \frac{\partial}{\partial \phi}(Avw) + \delta rw(u\cos\phi - v\sin\phi)\right]$$
$$= -\frac{1}{A}\frac{\partial p}{\partial \theta} + \frac{1}{Re}\left\{\frac{1}{rA}\left[\frac{\partial}{\partial r}\left(rA\frac{\partial w}{\partial r}\right) + \frac{\partial}{\partial \phi}\left(\frac{A}{r}\frac{\partial w}{\partial \phi}\right)\right] - \frac{\delta^2}{A^2}w\right\}, \tag{4}$$

$$\frac{1}{rA}\left[\frac{\partial}{\partial r}(rAu) + \frac{\partial}{\partial \phi}(Av)\right] = 0, \tag{5}$$

$$A = 1 + \delta r\cos\phi$$

where a, R, U, ν, and ω are the tube radius, the radius of curvature, the maximum axial velocity averaged over the cross-section, the kinematic viscosity of the fluid, and the angular frequency of pulsation in a systole, respectively, $\delta = a/R$, Re is the Reynolds number, defined as $Re = aU/\nu$, and $\alpha = a(\omega/\nu)^{1/2}$. Dimensionless forms of the above equations can be written by substituting

$$(u, v, w) = \left(\frac{u'}{U}, \frac{v'}{U}, \frac{w'}{U}\right), \quad p = \frac{p'}{\rho U^2}, \quad r = \frac{r'}{a}, \quad t = \omega t' \tag{6}$$

where $'$ represents dimensional values.

2.2. *Numerical methods*

Simulations were made for only a half-cross-section, because the flow field is assumed to be symmetric with respect to the (x, z)-plane (figure 1). The semicircular section is divided into 30×30 control volumes. Periodic unsteady flow at high α causes steep velocity gradients near the wall, which therefore requires a non-uniform grid in the radial direction, with finer grid spacing near the wall. The grid spacing is uniform in the circumferential direction. Figure 2 shows the grid used in our simulations. The radial position of the ith control-volume face r^u and the grid point r^m is

$$\left.\begin{aligned} r_i^u &= 1 - \frac{\exp\left(\beta \times \dfrac{31 - \mathrm{i}}{30}\right) - 1}{\exp(\beta) - 1} \qquad (\beta = 2), \\ r_i^m &= (r_{i+1}^u + r_i^u)/2. \end{aligned}\right\} \tag{7}$$

A staggered grid was used, where the scalar variables were stored at the main grid points and the velocities were stored at the control-volume faces, as shown in figure 3.

https://doi.org/10.1017/S0022112097006538 Published online by Cambridge University Press

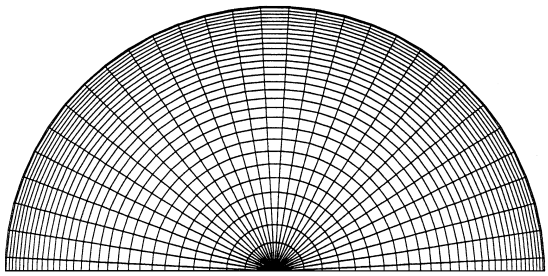


FIGURE 2. Grid system of axial velocity and pressure in cross-section.

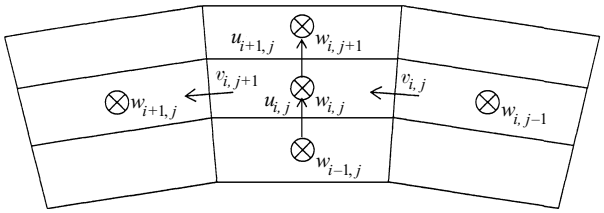


FIGURE 3. Staggered grid.

Finite-difference approximations to the partial derivatives were made, and the convective terms were discretized by the power-law scheme and the relation between pressure and flow was treated with the SIMPLER algorithm (Patankar 1981). The power-law scheme gives velocities on the boundaries of control volumes using a function that is proportional to the fifth power of a local one-dimensional Péclet number, which itself is a function of the normal velocity to the control-volume face and the local diffusion coefficient. The power-law scheme is an economical approximation to the exact one-dimensional transport solution in a control-volume. It is superior to the up-wind scheme because the effect of the artificial viscosity is reduced, enabling complicated flow structures with reversed flow and small vorticies to be accurately simulated.

The ILUBCG (Wilkinson & Reinsh 1971) and SOR methods were used to calculate the pressure. The pressure is solved by an iterative estimator/corrector technique, and the iterative solution continues until the absolute value of pressure is invariant to six significant figures. The convergence rate of this iterative solution using the ILUBCG method is sufficient down to five significant figures, but then deteriorates. Therefore, after the iterative solution produces pressures that are stable down to five significant figures, the SOR method is used to obtain a solution of the pressure equation that is invariant to six significant figures. The calculation was continued over several pulsation periods until an oscillatory steady state was achieved. The convergence criterion for the velocity calculation was that the maximum change in velocity in an iteration was less than 10^{-4}, and was calculated as follows

$$\mathrm{Max}\,(|(\boldsymbol{u}^{n+1} - \boldsymbol{u}^{n})/\boldsymbol{u}^{n}|) < 10^{-4}. \tag{8}$$

The intermittent flow waveform was given by (figure 4)

$$\left.\begin{aligned} Q^{k} &= \sin(k \times \Delta t) \quad (0 \leqslant k \times \Delta t < \pi) \\ &= 0 \qquad\qquad\quad (\pi \leqslant k \times \Delta t < \pi/\eta). \end{aligned}\right\} \tag{9}$$

We cannot give the flow-rate condition explicitly in the discretization equations.

https://doi.org/10.1017/S0022112097006538 Published online by Cambridge University Press

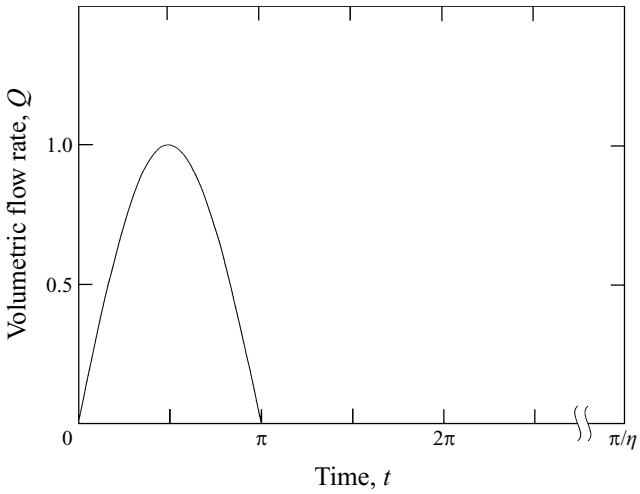


FIGURE 4. Flow waveform.

The pressure gradient was predicted and corrected so as to satisfy the condition of flow rate. For each period of intermittent flow, 128 $\sim$ 240 time steps were used.

2.3. *Boundary conditions*

The non-slip boundary condition was used on the wall, and the gradients of all physical variables with respect to ϕ at $\phi = 0$ and π were set equal to zero (i.e. symmetry assumption).

In the coordinate system used in this work, there is a singular point at the centre of the tube. Therefore, we evaluated the radial velocity at the centre using an interpolation of the neighbouring points, rather than including the centre point in the discretization equations.

In our grid system, the shape of most of the control volumes are trapezoids, and the neighbour discretization coefficients ($\boldsymbol{u}_i$: $i = n, e, w, s$) are calculated from the geometry of each control volume and the normal velocity component on each face of the control volume ($\boldsymbol{u}_N$, $\boldsymbol{u}_S$, $\boldsymbol{v}_E$ and $\boldsymbol{v}_W$). For the radial velocity, the control volume closest to the centre is a trapezoid (figure 5*a*) and one of the neighbouring grid points is singular. Therefore the velocity on the symmetry line, U_0, is linearly interpolated from values of the neighbouring grid points, and the radial velocity in each direction is given by $U_0 \cos(\phi)$. On the other hand, control volumes for axial and circumferential velocities are triangles (or trapezoids having an upper base of zero length). Figure 5(*b*) shows the grid for the axial velocity. A point of u_S is also singular, but we do not need to consider the effect from this direction since this edge has no length. In fact, the coefficients for w_s and v_s in the discretization equations are always zero for these control volumes. Therefore, we do not give boundary condition for w and v explicitly at the centre of tube, and the equations for w and v are integrated without the values u_S, w_s, and v_s at the centre cell:

$$\left.\begin{array}{lll} \dfrac{\partial u}{\partial \phi} = 0,\ v = 0 & \text{at} & \phi = 0, \pi, \\ u = v = w = 0 & \text{at} & r = 1, \\ u = U_0 \cos(\phi) & \text{at} & r = 0. \end{array}\right\} \tag{10}$$

https://doi.org/10.1017/S0022112097006538 Published online by Cambridge University Press

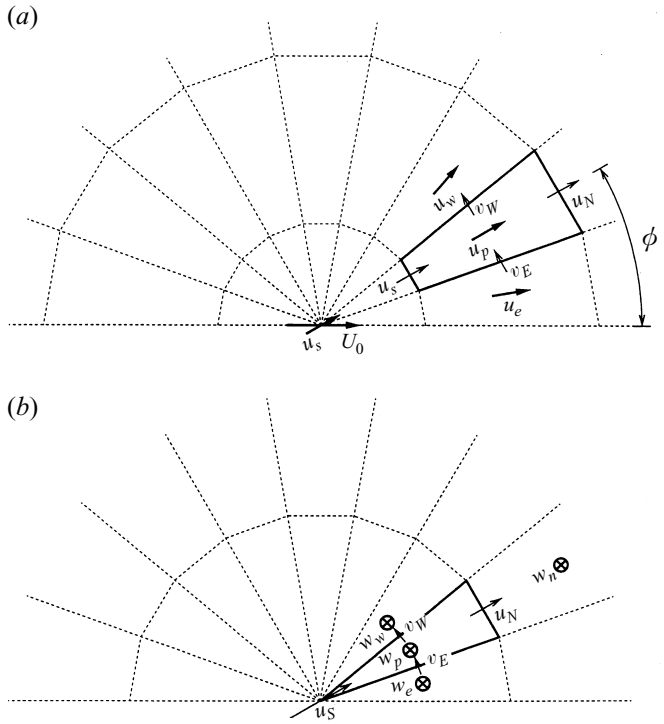


FIGURE 5. Control volumes near the centre. (*a*) Radial velocity, (*b*) axial velocity.

2.4. *Numerical procedure*

To reduce the computational effort, coarse-grid solutions were solved first, and these solutions were used as the starting values for fine-grid solutions. In some cases the finer-grid solutions were obtained with and without the coarse-grid solutions (all values were initialized by zero), which reached identical oscillatory steady state conditions.

The numerical procedure is as follows. We iterate the SIMPLER procedure within each time step until the convergence criterion for the relative change of every velocity component is less than 10^{-5}. The equations are integrated using the fully-implicit method. For $\eta = 0$, which simulates starting/stopping flow, the calculation starts with the static flow condition ($\boldsymbol{u} = 0$) at $t = 0$ and proceeds to 5π. For $\eta \neq 0$, we need about 200 cycles to reach oscillatory steady state for initial values of 0 for all of the variables.

The procedure is outlined in the flow chart in figure 6.

2.5. *Grid and time-step dependency*

To determine the optimum number of grid points, N, and the optimum time step for these simulations, we made a preliminary calculation under the conditions of $\eta = 1/5$, $\kappa = 393$, $\alpha = 27$, $\delta = 1/2$, and $16 \leqslant N \leqslant 34$.

Figure 7 shows the axial and secondary velocity profiles at $t = \frac{1}{2}\pi$ and 2π. The profiles in the upper half of the cross-section show streamlines of the secondary flow and the profiles in the lower half show contours of the axial velocity. Solid, dotted and dot-dash lines in the lower panel indicate positive, zero and negative values respectively. With our code, the axial and secondary flow profiles are nearly

https://doi.org/10.1017/S0022112097006538 Published online by Cambridge University Press

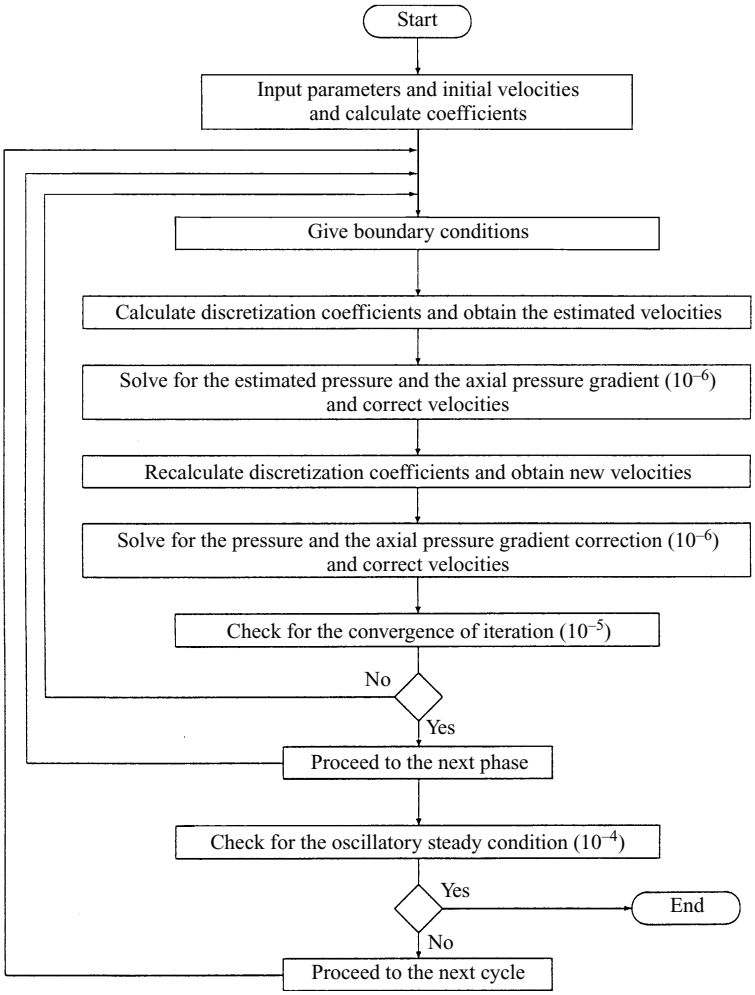


FIGURE 6. Flow chart of the numerical algorithm.

independent of the grid size except for the streamlines of the secondary flow at $t = \frac{1}{2}\pi$; the centre of the secondary flow vortex moves slightly toward the inner wall as N increases up to 34. However, the profile of the streamline for $N = 30$ is identical to that for $N = 34$. In order to quantitatively verify the grid dependence of the resultant velocity profile, we checked the maximum axial velocity W_{max} and maximum stream function of the secondary flow, Ψ_{max}, for each grid, as shown in figures 8 and 9. W_{max} becomes grid-independent for $N \geqslant 30$ at $t = \frac{1}{2}\pi$, 2π, and 5π. In figure 9, Ψ_{max} increases slightly with increasing N, but the rate of increase decreases for $N \geqslant 30$, and is only 1.2% larger at $N = 34$ than at $N = 30$. To minimize simultaneously both the grid dependency and the computational time, we choose $N = 30$.

Time-step dependency was verified for $\Delta t = \pi/24$, $\pi/48$, and $\pi/96$ using the same flow parameters as for the grid-dependency check and $N = 30$. For $\Delta t = \pi/24$, $\pi/48$ and $\pi/96$ the predicted values of W_{max} at $t = 2\pi$ and Ψ_{max} at $t = 0.8541\pi$ agreed to within four significant figures, and Ψ_{max} at $\Delta t = \pi/24$ was 2.3% lower than Ψ_{max} at $\Delta t = \pi/48$ at most. Considering the time-step dependency as well, we choose $\Delta t = \pi/64$–$\pi/48$, which divides the entire period into 128–240 time steps.

https://doi.org/10.1017/S0022112097006538 Published online by Cambridge University Press

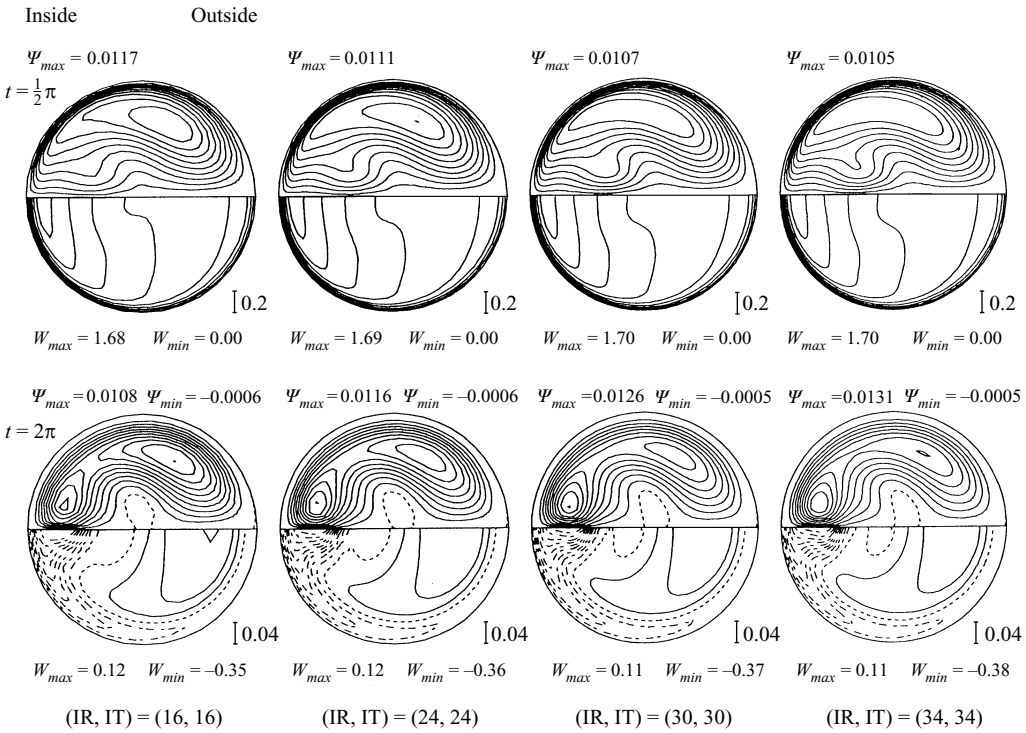


FIGURE 7. Flow profiles as a function of grid size.

3. Results

3.1. *Reliability of the numerical procedure*

To check the reliability of our numerical procedure, we simulated two kinds of oscillatory flow in a curved tube. The first flow condition was $\alpha = 10$, $Re = 100$, and $\delta = 0.3$ ($\kappa = Re\delta^{1/2} = 54.8$), which is identical to the condition used in the work by Eckmann & Grotberg (1988). Figure 10 shows a comparison of our simulated axial velocity distributions on the plane of symmetry with the experimental data of Eckmann & Grotberg (1988). The data compare well except for the velocity near the inner wall. Since the axial flow near the inner wall is more sensitive to the curvature in oscillatory flow than the flow near the outer wall, the discrepancy appearing near the inner wall may be due to the small curvature approximation (i.e. $\delta \ll 1$) assumed in the perturbation method of Eckmann & Grotberg (1988). The second flow condition is $\alpha = 18$, $Re = 133$ and $\delta = 1/2$ ($\kappa = 94$). The numerical results are shown in figure 11, and agree well with the LDV measurements of Naruse *et al.* (1990*a*). The accuracy of the numerical procedure is therefore validated against experimental results.

3.2. *Conditions of numerical simulations*

The numerical simulations were carried out under the conditions listed in table 2. As previously defined, the intermittency parameter η is defined as the ratio of the systolic period to the entire period, and $\eta = 0$ corresponds to complete starting/stopping flow. Since the flow waveform in the systolic period is that of forward flow in a sinusoidal oscillatory flow, the periodicity of the flow variation is expressed by two kinds of Womersley numbers; α and $\hat{\alpha}$. The Womersley number α is based on flow where the sinusoidal period is twice that of the systolic period, and the Womersley

https://doi.org/10.1017/S0022112097006538 Published online by Cambridge University Press

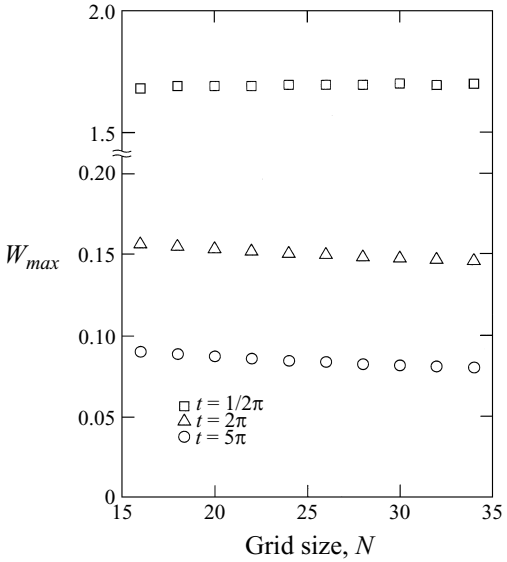


FIGURE 8. Maximum axial velocity as a function of grid size.

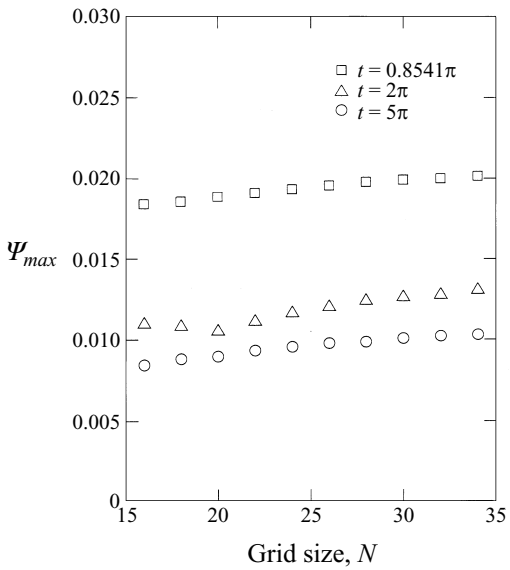


FIGURE 9. Maximum secondary flow stream function as a function of grid size.

number $\hat{\alpha} = (2\eta)^{1/2}\alpha$ is based on the pulsatile cycle period. The combination of α and η are sufficient to describe the effect of intermittency on the flow field, and in this study we only use α for discussing the flow phenomena.

Profiles of the axial and secondary velocity and calculated transverse pressure are shown in figures 12–17. The streamlines of the secondary flow are shown in the upper half of the cross-section and axial-velocity contours are shown in the lower half. The value of the stream function is defined as zero on the wall and positive in the counterclockwise vortex.

https://doi.org/10.1017/S0022112097006538 Published online by Cambridge University Press

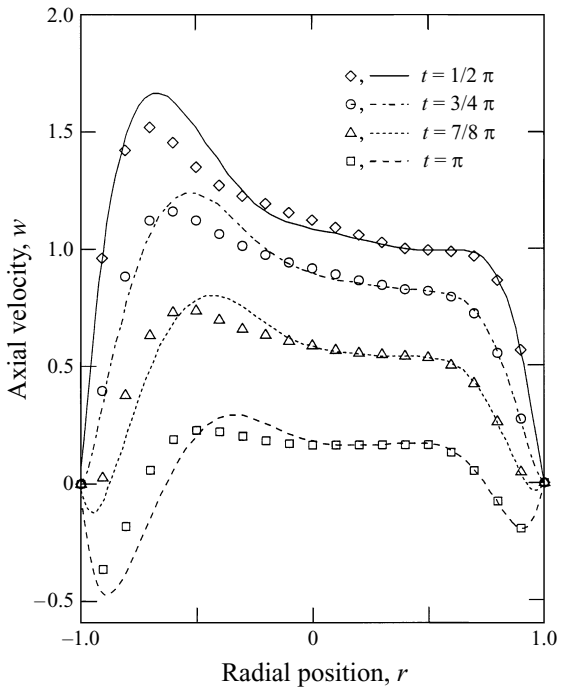


FIGURE 10. Comparison of fully developed axial velocity on the plane of symetry for $\delta = 0.3$, $\kappa = 54.8$, $\alpha = 10$, lines: present calculation, symbols: Eckmann & Grotberg (1988).

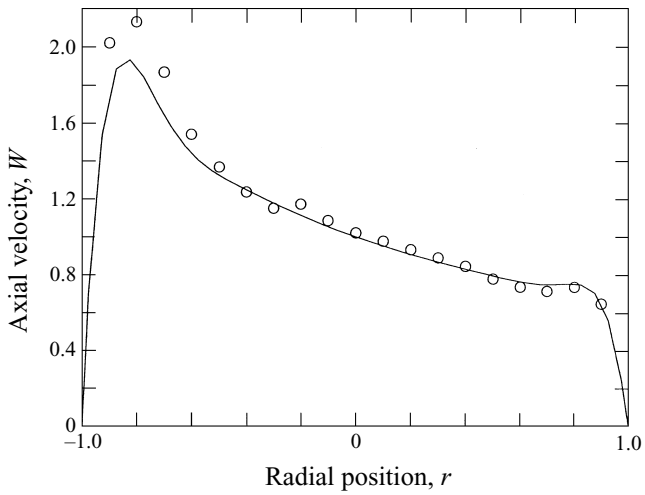


FIGURE 11. Comparison of fully developed axial velocity on the plane of symetry for $\delta = 1/2$, $\kappa = 94$, $\alpha = 18$, $t = \frac{1}{2}\pi$; ○, measured by Naruse *et al.* (1990*a*); ——, present calculation.

3.3. *Velocity profiles*

Figure 12 shows the velocity profiles for $\eta = 0$, $\kappa = 393$, $\alpha = 27$, and $\delta = 1/2$. The flow waveform of $\eta = 0$ is starting/stopping flow: the flow rises from the stationary state and then stops. In the systolic period ($t = 0$–π), the velocity contours in the core region are uniform and the maximum axial velocity occurs near the inner wall. This profile indicates that the flow field is potential flow dominated by inertia. The effect

https://doi.org/10.1017/S0022112097006538 Published online by Cambridge University Press

κ	α	δ	Re	η
393	4	1/2	556	0, 1/5, 1/3
393	8	1/2	556	0, 1/5, 1/3
393	18	1/2	556	0, 1/5, 1/3
393	27	1/7	1040	1/5
393	27	1/3	681	1/5
393	27	1/2	556	0, 1/5, 1/3, 1/2

TABLE 2. Parameter values used for the flow simulations

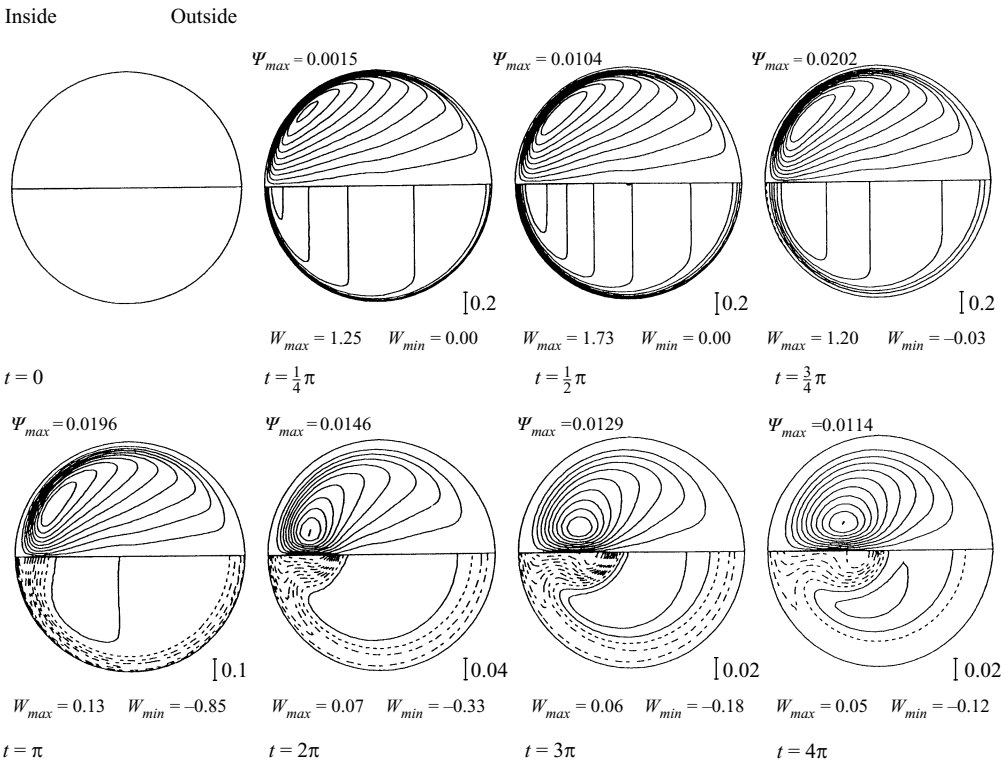


FIGURE 12. Secondary flow streamlines and axial velocity contours for $\eta = 0$, $\kappa = 393$, $\alpha = 27$, $\delta = 1/2$.

of viscosity is restricted to a thin boundary layer near the wall, because of the high frequency parameter, and the secondary flow has not yet developed well after starting from the resting condition. The axial velocity profile resembles a potential vortex, in which the axial velocity is inversely proportional to the distance from the centre of curvature. The fact that the core region has steep axial-velocity gradients was observed experimentally by Naruse *et al.* (1990*a*) in oscillatory flow profiles with $\alpha = 18$ and $\delta = 1/2$. Therefore, the axial flow profiles strongly depend on the curvature ratio, δ. In a gently curved tube, the axial-velocity gradient becomes flat as in the physiological flow for $\alpha = 20.76$, $\delta = 1/10$, and $Re = 3300$ shown by Chandran & Yearwood (1981). In the circumferential Stokes layer, the secondary flow accelerated towards the inner wall and reached a maximum velocity at $\phi = 132°$. Accordingly, the centre

https://doi.org/10.1017/S0022112097006538 Published online by Cambridge University Press

of the secondary flow vortex appears near the location of the maximum secondary flow velocity.

During the stationary period ($t = \pi-$), reversed axial velocity appears in the circumferential wall region. The appearance of the reversed flow near the wall characterizes the stopping flow (Weinbaum & Parker 1975). In stopping flow, the axial flow rate rapidly decreases to zero at $t = \pi$ while maintaining the same relative velocity profile, causing the fluid near the wall to reverse direction. The boundary layer is circumferentially constructed by the reversed axial flow, and the secondary flow streaming into the inner corner protrudes as a jet toward the outer wall. With increasing time in the diastolic phase, both forward and reverse flow in the cross-section gradually decay to zero due to energy dissipation. The reduction of centrifugal force due to the decreasing axial velocity lowers the strength of the secondary flow, and simultaneously the weakened secondary flow vortex moves toward the centre of the half-cross-section and the reversed axial flow region is enlarged by the secondary flow. The secondary-flow stream function shown in figure 18 illustrates the process during the diastolic phase.

Figure 13 shows the flow profiles for $\eta = 1/5$, $\kappa = 393$, $\alpha = 27$, and $\delta = 1/2$ ($\eta = 1/5$ means that the period of the systolic phase is $1/5$ of the entire cycle period). At the end of the diastolic phase, the axial and secondary velocity components persist, so that they become the initial velocity profile for the following period. In this regard, the velocity profile at the end of the diastolic phase is a key factor for determining the velocity variation during the entire period. Figure 13 shows two secondary vortices appearing in the half-cross-section at $t = 0$, and the reversed axial flow occupies almost the entire inner half of the cross-section. During the maximum-velocity phase (i.e. $t = \frac{1}{2}\pi$), a thin Stokes layer develops near the wall, where the fluid is accelerated toward the inner wall along the circumferential direction due to the strong pressure gradient. The secondary-flow vortex growing due to the strong acceleration near the wall shifts toward the inner wall, and the other vortex stemming from the residual vortex at the end of the previous diastolic phase decays and disappears at $t = \frac{1}{2}\pi$. This process is more clearly shown in figure 14 in terms of the secondary flow vector and the pressure. The upper half of figure 14 shows vectors of the secondary flow and the lower half shows contours of transverse pressure. The secondary flow velocity inside the Stokes layer is accelerated but that in the core is decelerated from an earlier systole (i.e. $t = \frac{1}{4}\pi$). The residual secondary flow of the previous period outside the Stokes layer is overcome by the mean flow acceleration. After the acceleration of the Stokes layer, at $t = \frac{3}{4}\pi$ the secondary flow in the core region starts increasing. The developed secondary vortex is very similar to that observed in figure 12.

In the beginning of the diastolic phase (i.e. $t = 2\pi$), the nature of the stopping flow characterizes the resulting velocity profiles. The boundary layer is circumferentially constructed by the reversed axial flow and the jet-like secondary flow appears near the inner wall at the beginning of the diastolic phase. The jet-like secondary flow causes another vortex, and the secondary flow governs the flow field in the diastole. As observed in figure 14, while the pressure field in a systole is caused by the axial velocity, in a diastole it is caused by the secondary flow, where the minimum of the pressure occurs at the centre of the vortex. Furthermore, the secondary-flow stream forms a stagnation flow which generates another small vortex with counterclockwise rotation, indicated by A in figure 13. This vortex is similar to that of the Lyne (1971) type which appears in oscillatory flow in curved tubes. Since there is no pressure gradient around the vortex (i.e. figure 14), the driving force is viscosity from another secondary-flow vortex. During the diastolic period, the boundary layer consisting of

https://doi.org/10.1017/S0022112097006538 Published online by Cambridge University Press

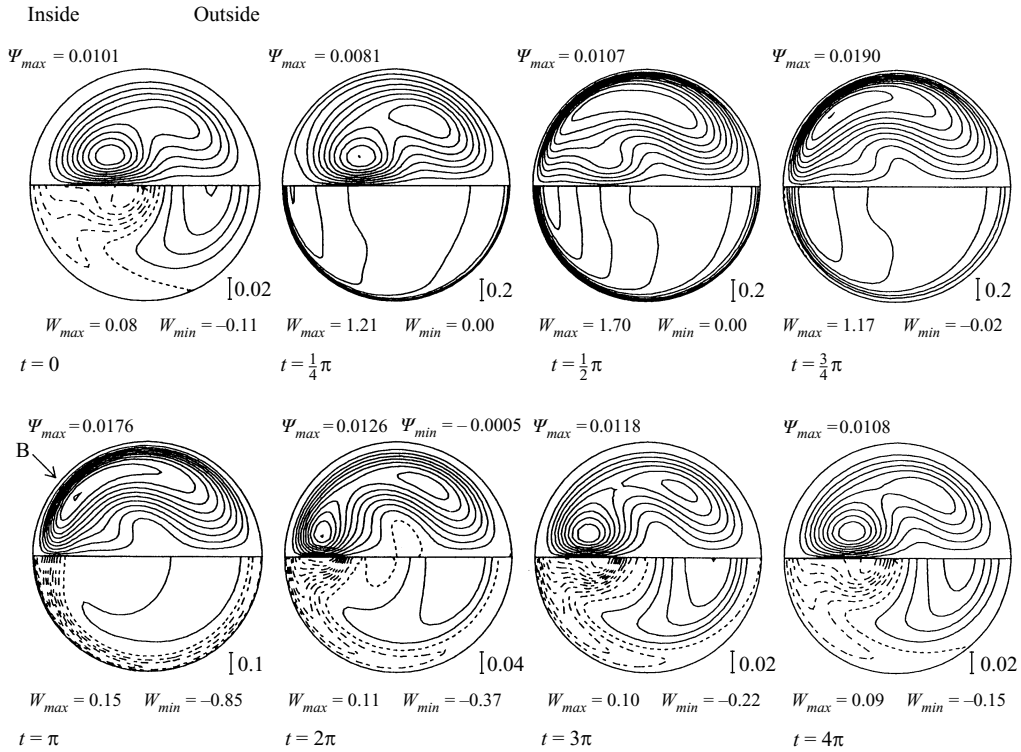


FIGURE 13. Secondary flow streamlines and axial velocity contours for $\eta = 1/5$, $\kappa = 393$, $\alpha = 27$, $\delta = 1/2$.

reversed axial flow grows further by interacting with the secondary flow. Because of the secondary flow, the boundary layer is extended toward the centre of tube and the secondary flow is locally strengthened (i.e. see the progression from 2π to 4π in figure 14). In this process, the secondary flow vortex appearing at the beginning of the diastole also moves toward the centre of tube. On the other hand, another secondary vortex gradually diminishes due to the lack of energy supply from the main flow.

Figure 15 shows the flow profiles for $\eta = 1/3$, $\kappa = 393$, $\alpha = 27$, and $\delta = 1/2$. A secondary flow vortex maintains almost a constant profile during the entire period, but the secondary flow is locally accelerated with development of the axial flow boundary layer in the diastolic phase. In this flow condition, the induced secondary flow during a diastolic phase does not create an additional vortex, but forms the stagnation area of the secondary flow at $t = \frac{3}{2}\pi$, shown by A in figure 15. Furthermore, it is very interesting that the secondary flow is induced in a different way from other flow conditions. Since the secondary flow near the inner wall is weak at the beginning of the diastole as compared to other conditions of higher intermittency $\eta = 0$ and $1/5$, the jet-like secondary flow appears with a longer delay, as indicated by B in figure 15, but the maximum of the secondary velocity continues to increase from $t = 1.71\pi$, even in a diastole. The time variation of the strength of the secondary flow is shown in figure 19.

The velocity profiles for $\eta = 1/2$ are shown in figure 16. Because the diastolic period is shorter than for $\eta = 1/5$ (figure 13), the velocity profile is strongly altered. The diastolic period is so short that the boundary layer does not develop sufficiently

https://doi.org/10.1017/S0022112097006538 Published online by Cambridge University Press

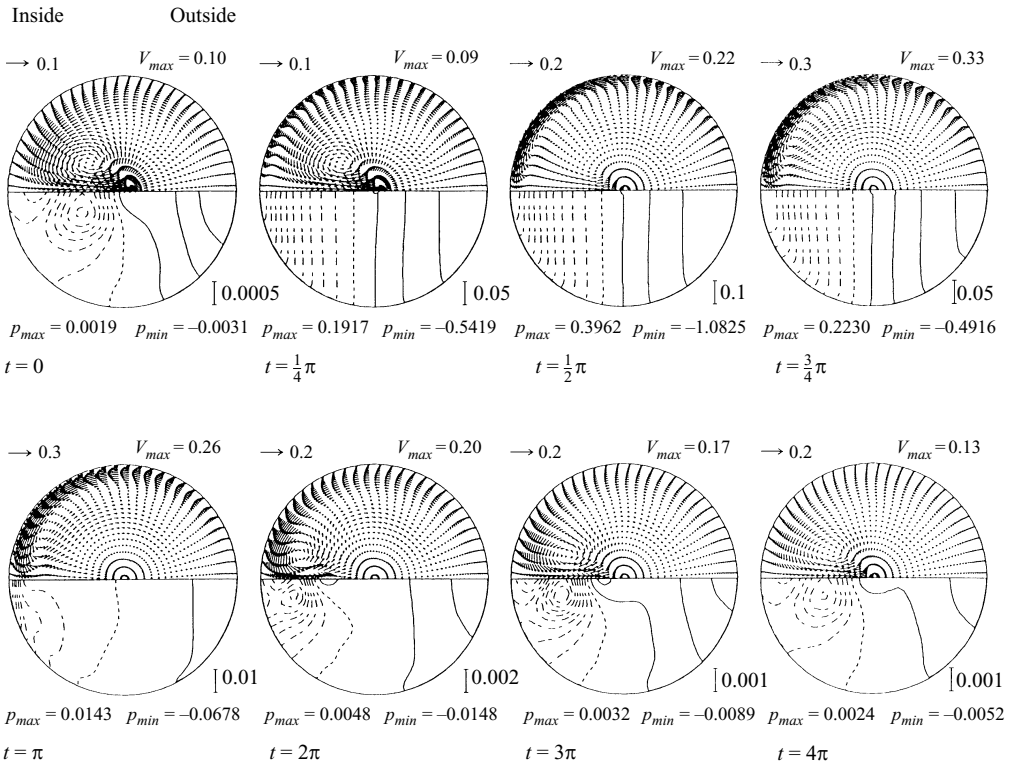


FIGURE 14. Secondary flow vectors and pressure contours for $\eta = 1/5$, $\kappa = 393$, $\alpha = 27$, $\delta = 1/2$.

until the end of diastolic phase, and this allows the invisid core to remain in the cross-section. The secondary flow in the core region is uniformly directed towards the outer wall. The strong secondary flow, being similar to that observed in figure 13, is generated circumferentially along the tube wall. Then the centre of this vortex approaches the circumferential position of $\phi = 82^\circ$ at $t = 2\pi$ and the secondary flow in the inviscid core is nearly uniform toward the outer wall. Note that the axial velocity profile in the core region does not have uniform gradients from the outside wall to the centre during a systolic phase, which differs from the potential vortex pattern observed for $\eta = 0$. At the end of the systolic period, the maximum axial velocity appears near the outer wall with the presence of a reversed boundary-layer region. With increasing time, the boundary layer progressively grows; however, the velocity profile in the core region is not altered, and persists to the end of the diastolic period, becoming the initial velocity profile in the beginning of the following systolic phase.

Figure 17 shows the velocity profile with lower α (i.e. $\eta = 1/3$, $\kappa = 393$, $\alpha = 8$, and $\delta = 1/2$). The decrease of α means that the time required for transport of viscous effects becomes shorter compared to the entire period, approaching a quasi-steady state. In the flow acceleration phase, the maximum axial velocity shifts toward the inner wall, exhibiting similar velocity profiles as starting/stopping flow (i.e. $\eta = 0$). In the flow deceleration phase the maximum velocity moves toward the outer wall. In the diastolic phase the boundary layer starts to develop, inducing the additional secondary flow. The region of reversed axial velocity appears in the inner half-cross-section, then this region shifts toward the outer wall due to the presence of secondary

https://doi.org/10.1017/S0022112097006538 Published online by Cambridge University Press

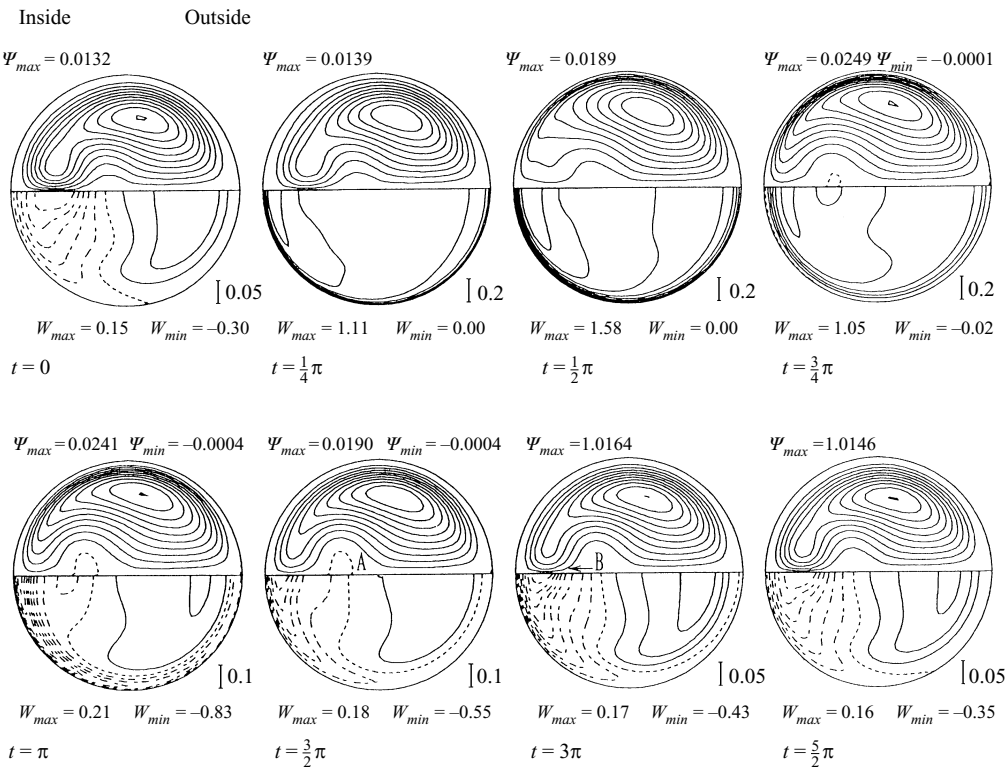


FIGURE 15. Secondary flow streamlines and axial velocity contours for $\eta = 1/3$, $\kappa = 393$, $\alpha = 27$, $\delta = 1/2$.

flow, although the velocity itself gradually decreases. In our calculations, the effect of the intermittency does not appear for $\alpha \leqslant 8$. Two reasons for this behaviour are suggested. One reason is the low magnitude of the residual flow at the beginning of a systole. Even for a high intermittency parameter (i.e. $\eta = 1/2$), the velocity component diminished almost completely during a diastole, with $W_{max} = 0.06$ and $W_{min} = -0.06$ for $\alpha = 8$. The other reason is the quasi-steadiness of the flow field. In a quasi-steady condition, the flow field is less sensitive to the initial conditions but is more sensitive to instantaneous changes in the viscosity and axial pressure gradient.

The variation of flow profiles in a period indicates the significant role of the intermittency in flow development, and two dominant factors cause the variation of flow profile for moderately high frequency ($\alpha > 8$). The first dominant factor is strong acceleration of the main flow caused by unsteady axial pressure gradients. The second factor is the development of a new boundary layer caused by the stopping flow and by the locally accelerated secondary flow. The diastolic duration is sufficiently short so as to preserve the flow at the end of the diastole, which, in turn, becomes the initial flow condition for the next systole. Therefore, the intermittency strongly affects the flow development over the entire period.

3.4. *Strength of secondary flow*

The velocity profiles of the intermittent flow in a curved tube are strongly dependent on the initial velocity profiles, which have a residual secondary flow component at the beginning of the systolic phase. The secondary flow variation can be characterized

https://doi.org/10.1017/S0022112097006538 Published online by Cambridge University Press

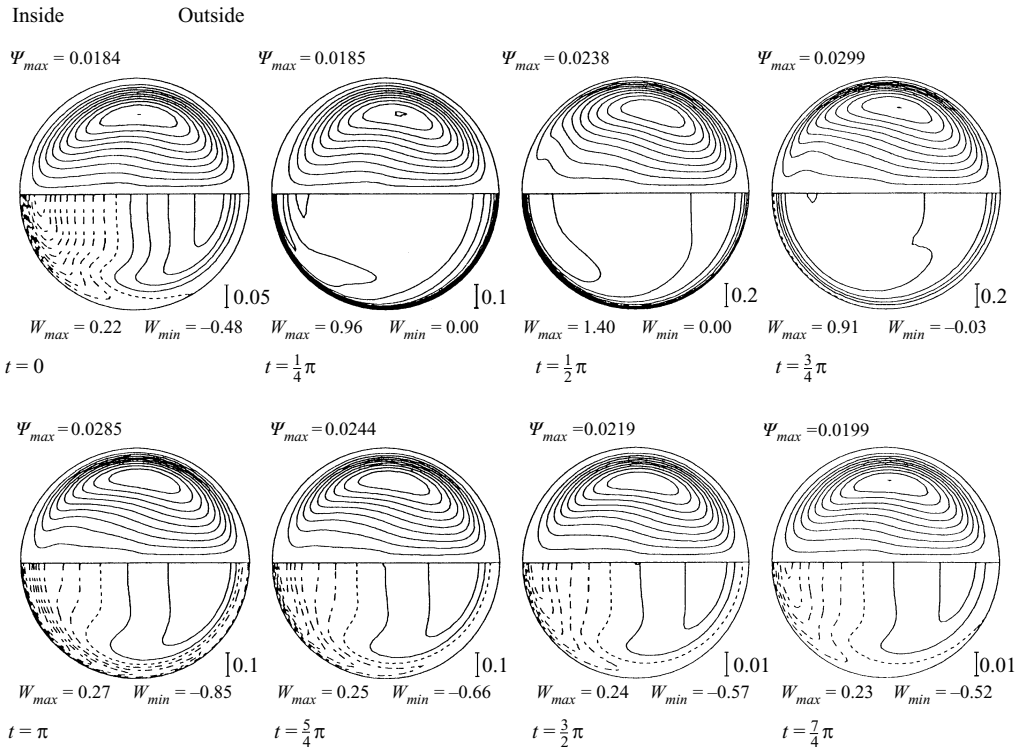


FIGURE 16. Secondary flow streamlines and axial velocity contours for $\eta = 1/2$, $\kappa = 393$, $\alpha = 27$, $\delta = 1/2$.

by the maximum stream function of the secondary flow and the maximum secondary velocity in the cross-section, as shown in figures 18 and 19. The definition of the stream function of the secondary flow is described in the Appendix.

Figure 18 shows the variation of the maximum stream function of the secondary flow with respect to time, and 'osc' refers to the maximum stream function in the sinusoidally oscillatory flow with a period of 2π. In the starting/stopping flow (i.e. $\eta = 0$) the maximum stream function increases rapidly from zero in the accelerating phase and reaches a maximum immediately before the end of the systolic phase. In the stationary phase the maximum stream function does not show a sudden drop, but decreases slowly. For $\eta > 0$, the initial value of the stream function at the beginning of the systolic phase increases with increase of η. The increase of η means the reduction of the diastolic period, during which the overall velocity dissipates. The magnitude of the residual secondary flow is therefore inversely proportional to the length of the diastolic phase. As soon as the flow starts to accelerate at the beginning of the systolic phase, the secondary flow profiles are reconstructed from the residual secondary flow vortex. The Stokes layer is circumferentially constructed in an early systole, and secondary flow inside the layer is accelerated, but the flow outside the layer, which also makes up the residual vortex, decelerates, as shown in figure 14. This process causes a slight delay of the increase in the stream function during the beginning of the systolic phase.

The rate of decrease of the stream function during the diastolic phase also depends on η. For $\eta = 0$, the secondary flow vortex developed in the systolic phase changes

https://doi.org/10.1017/S0022112097006538 Published online by Cambridge University Press

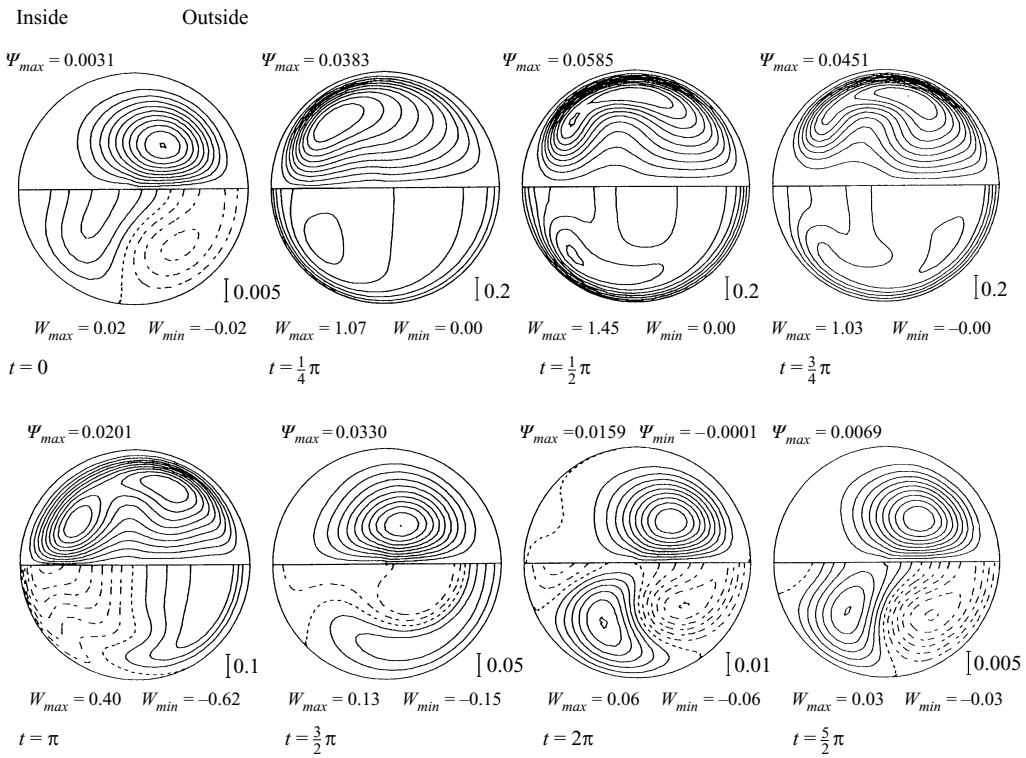


FIGURE 17. Secondary flow streamlines and axial velocity contours for $\eta = 1/3$, $\kappa = 393$, $\alpha = 8$, $\delta = 1/2$.

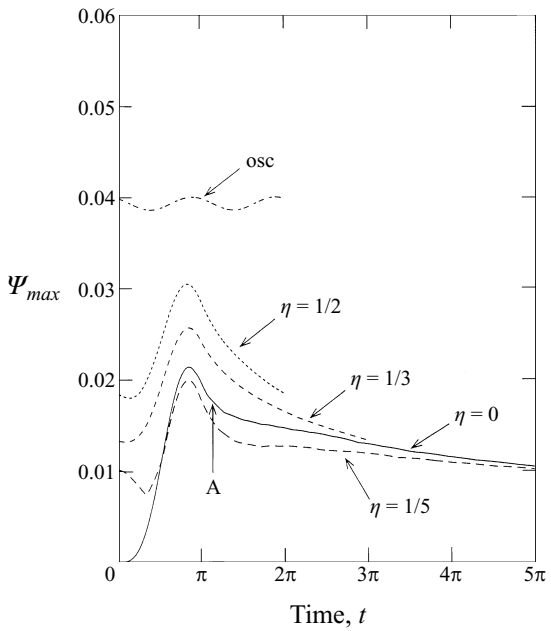


FIGURE 18. Variation of maximum of secondary flow streamfunction for $\kappa = 393$, $\alpha = 27$, $\delta = 1/2$.

https://doi.org/10.1017/S0022112097006538 Published online by Cambridge University Press

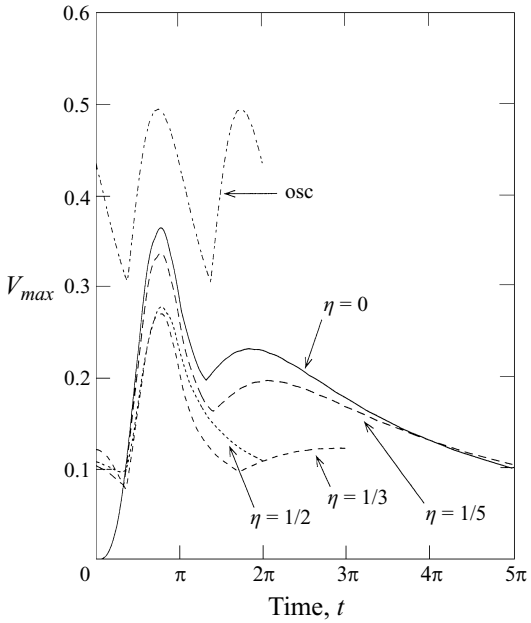


FIGURE 19. Variation of maximum of secondary velocity for $\kappa = 393$, $\alpha = 27$, $\delta = 1/2$.

to a vortex characterized by the stopping flow at the beginning of the diastolic phase. The shift of the vortex feature is identified by the discontinuity of the stream function gradient at $t = 1.16\pi$, indicated by A in figure 18. For $\eta = 1/5$, two kinds of vortices appear in the diastolic phase, and the gradient of the stream function shows a discontinuity at $t = 1.35\pi$. The instant $t = 1.35\pi$ becomes identical to the phase when the strength of the new vortex overcomes the existing vortices. On the other hand, as shown in figures 15 and 16, for $\eta = 1/3$ and $1/2$ the gradient of the stream function does not have a discontinuity in the diastolic phase. The reversed axial flow in the boundary layer for $\eta = 1/3$ and $1/2$ still imposes a relatively large centrifugal force, inducing secondary flow in the diastolic phase, although its strength gradually decreases with increasing time.

The time variation of the maximum secondary flow velocity, V_{max}, shown in figure 19 is similar to the time variation of the maximum stream function shown in figure 18, but shows another aspect of the secondary flow development that is not observed in figure 18. In the acceleration phase, because of the strong acceleration, the maximum velocity occurs mostly in the circumferential boundary layer and the maximum velocity weakly depends on η. Contrary to the behaviour of Ψ_{max}, the peak of V_{max} increases with decreasing η. The secondary flow in a systole is driven by the transverse pressure gradient imposed by the axial velocity. For high η, reversed axial flow appearing at the inner corner at the end of a systole does not dissipate during a short diastole. Therefore, the axial velocity starts with reversed flow at the inner corner, which causes lower peak velocity than for low η. As a result, the maximum secondary velocity, which appears in the Stokes layer, decreases with increasing η.

In the diastolic phase, V_{max} does not decrease monotonically and exhibits an increase in the early stage of the diastolic phase. Notice that V_{max} shows a minimum even at $t = 1.71\pi$ for $\eta = 1/3$ and increases slightly until the next systole. Since the location of V_{max} varies in the cross-section and depends on the flow conditions,

https://doi.org/10.1017/S0022112097006538 Published online by Cambridge University Press

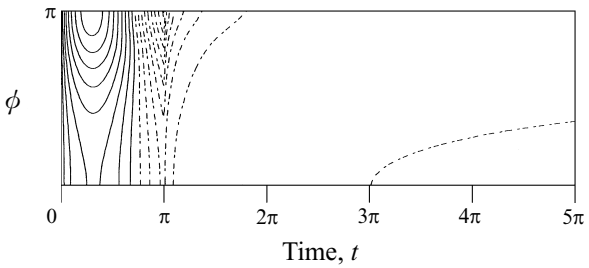


FIGURE 20. Contours of axial wall shear stress for $\eta = 1/5$, $\kappa = 393$, $\alpha = 27$, $\delta = 1/2$. Difference between lines is 10: ———, positive; — — —, zero; – – –, negative.

typically as a function of η, we must carefully interpret figure 18, particularly during the diastolic phase. For $\eta = 0$ and $1/5$, V_{max} appears at $\phi = 130°$ during the systolic phase, designated by B in figure 13. However, the location of V_{max} moves near the plane of symmetry during the diastolic phase. For $\eta = 1/3$, at the beginning of the systolic phase, the location of V_{max} is near the inner wall on the plane of symmetry, but moves to the circumferential region later in the systolic phase due to strong acceleration. Notice that the location of V_{max} at the beginning of the diastole stays in the circumferential region at $\phi = 90°$ until the later stage of the diastolic phase. However, the secondary flow locally induced at the inner corner (marked by B in figure 15) exceeds the secondary flow in strength in the circumferential region at $t = 1.71\pi$. Furthermore, for $\eta = 1/2$, V_{max} appears at $\phi = 90°$ during the entire cycle period.

3.5. *Wall shear stress*

The wall shear stress on the aortic arch is one of the significant factors affecting atherogenesis. Therefore, we discuss the effect of intermittent flow on the wall shear stress, which is a major factor in aortic arch flow. The non-dimensional wall shear stress is determined by the non-dimensional axial velocity at the nearest point to wall as

$$\tau = \frac{\partial w}{\partial r}. \tag{11}$$

Figure 20 shows the wall shear stress distribution for the conditions $\eta = 1/5$, $\kappa = 393$, $\alpha = 27$, and $\delta = 1/2$. The maximum wall shear stress appears at the inner wall in the acceleration phase (i.e. $t = 0.175\pi$) and the minimum stress (maximum negative shear stress) at the end of the systolic phase. The magnitude of the minimum shear stress is -41.65 and its absolute value is identical to that of maximum shear stress ($\tau_{max} = 44.14$). The wall shear stress decreases slowly from the inner to the outer wall in the circumferential direction. The absolute values of wall shear stress at the inner wall are much larger than at the outer wall during the cycle period, simply because of the thinner boundary layer in a systole and because of the presence of reversed flow in the boundary layer in a diastole. The maximum shear stress at the outer wall is 35% of that observed at the inner wall. In our results, the wall shear stress was only weakly affected by the length of a diastole. Though η increased from 0 to $1/2$, the maximum shear stress decreased by only 9.0% and the minimum decreased by only 0.38%. However, the important difference is that the change of shear stress at the inner wall became more abrupt as η increased. Namely, the shear stress for $\eta = 1/2$ at the end of the diastolic phase is still negative and abruptly changed

https://doi.org/10.1017/S0022112097006538 Published online by Cambridge University Press

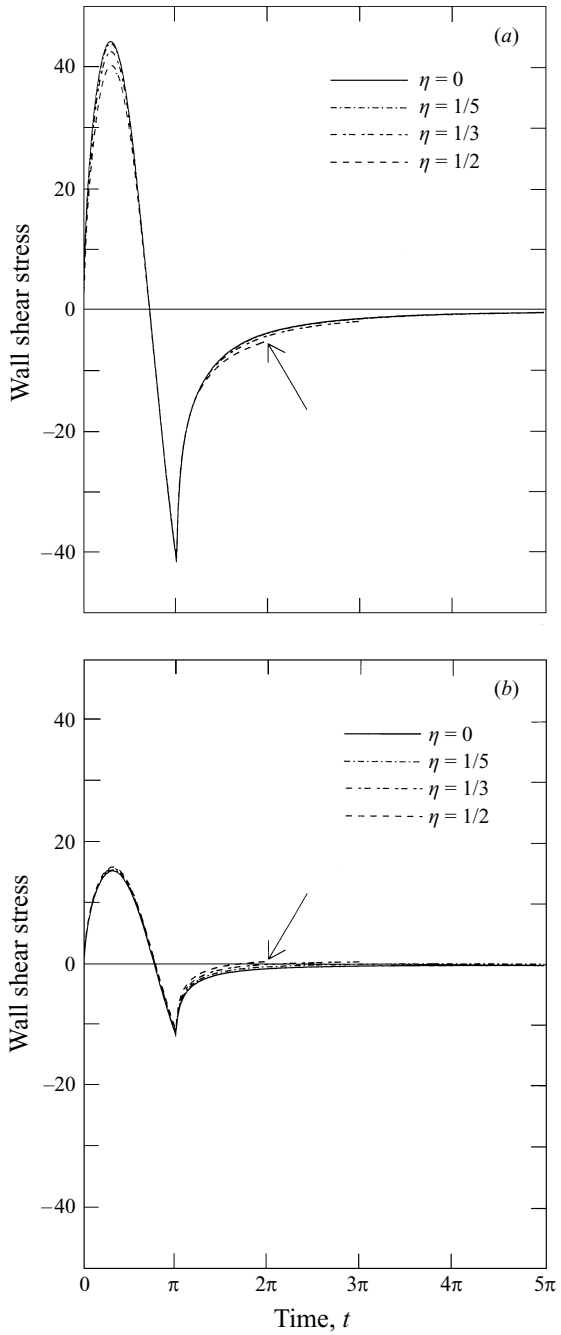


FIGURE 21. Variation of wall shear stress at (*a*) the inner wall and (*b*) the outer wall, for $\kappa = 393$, $\alpha = 27$, $\delta = 1/2$.

magnitude and direction. The time variation of the wall shear stress at the inner wall is shown in figure 21(*a*). On the other hand, the wall shear stress at the outer wall at the end of the diastolic phase was almost zero or slightly positive. Therefore, as shown in figure 21(*b*), a rapid change of magnitude and direction did not occur. Note that the time rate of change of the wall shear stress is significant at the inner wall

https://doi.org/10.1017/S0022112097006538 Published online by Cambridge University Press

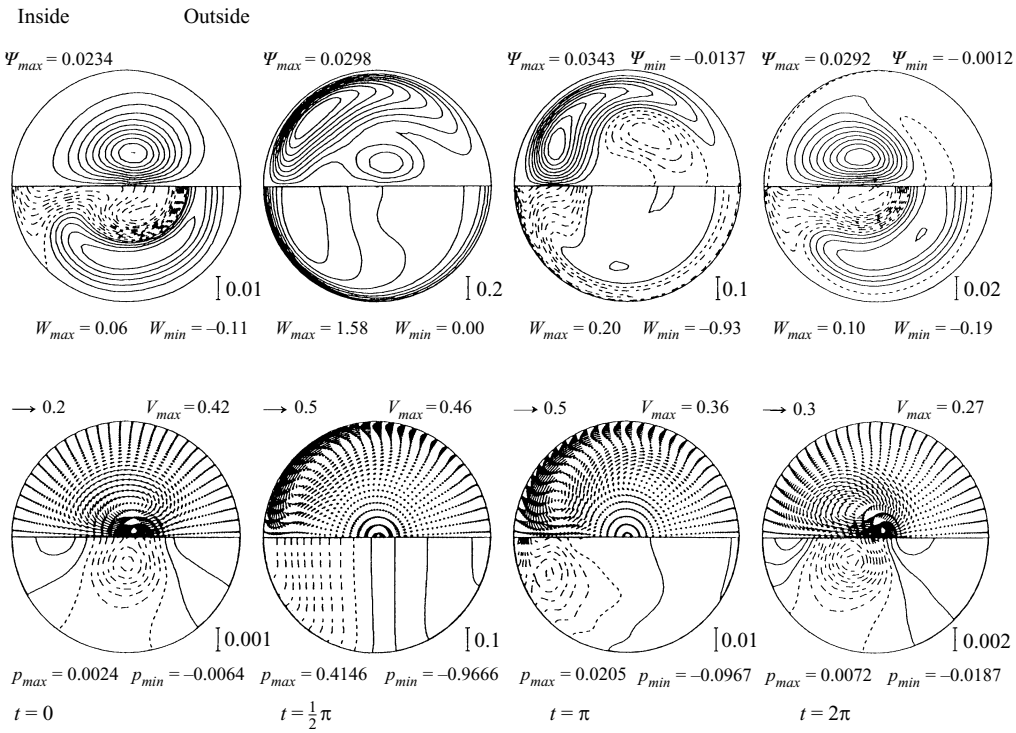


FIGURE 22. Various profiles of the flow field for $\eta = 1/3$, $\kappa = 393$, $\alpha = 18$, $\delta = 1/2$.

of the curved tube, the most frequently favoured sites of atherosclerotic lesions in intermittent oscillatory flow with large η. Ku *et al.* (1985) suggest the rapid change of direction of wall shear stress is one of the important factors causing atherosclerosis. The results of our numerical study show that the physiologically intermittent pulsatile flow also generates a rapid change of wall shear stress at the inner wall, as observed in the carotid artery by Ku *et al.* (1985). In connection with their study, the rate of change of wall shear stress may give a particular physical stimulus to the inner surface of the arterial wall, such as the stimulus to endothelial cells (Nerem 1992).

3.6. *Comparison with other flows*

The periodical flow with complete stationary period in a curved tube has not been studied previously; however, the physiological flow waveforms used in the numerical study by Chang & Tarbell (1985) are similar to the flow waveforms used in our study. In their physiological flow waveforms, the diastolic period was about half of the entire period and the average flow rate in a diastole was 6–12% of the peak flow in a systole. The flow condition IV in their paper is similar to our conditions, in which a high curvature ratio ($\delta = 1/3.8$) and a high frequency parameter ($\alpha = 18.58$) were used. Therefore, we need to compare our results for $\eta = 1/3$, $\kappa = 393$, $\alpha = 18$, and $\delta = 1/2$ with their condition IV. Figure 22 shows instantaneous streamlines of secondary flow and axial velocity contours in the upper row, and secondary flow vectors and transverse pressure contours in the lower row. Although the peak Dean number in the study of Chang & Tarbell was $\kappa = 1740$, which is much higher than ours, the overall flow structure of our numerical study is similar to theirs. The largest among the four vortices at the beginning of a systole in the work of Chang & Tarbell

https://doi.org/10.1017/S0022112097006538 Published online by Cambridge University Press

is similar to ours. In an early systole, the Stokes layer develops and a new vortex appears at the circumferential angle $\phi = 135°$, due to mechanisms similar to the ones we have discussed so far. Residual vortices also simultaneously coexisted. As shown in figure 20, in the deceleration phase of a systole, at $t = \pi$ a counterclockwise vortex appeared at the same position as ours. Our transverse pressure contours show flat profiles around the reversed vortex. We cannot compare our results with those of Chang & Tarbell during the development of a diastole, because they did not discuss their results during this phase. From our results, at the end of a systole a secondary vortex appeared, taking in newly induced secondary flow, and the position of the vortex shifted from the inside of the tube to the centre, by the same mechanism as discussed for the case of $\alpha = 27$.

Concerning the axial velocity, the results from both our study and Chang & Tarbell show negative, flat axial velocities on a symmetry plane near the inside, and positive ones near the outside. A recessed velocity profile is observed near the centre of tube. This recess is the result of acute reversed axial flow appearing near the inside at the end of a systole, which is conveyed toward the outside by the secondary flow during a diastole. The axial flow develops in a systole into a potential vortex profile with a recess. It is interesting that the characteristic phenomena of intermittent flow shown in our simulations are still valid in physiological flow, even though the peak Dean number is much higher (i.e. $\kappa = 1740$) and the flow condition in a diastole is not completely stationary (i.e. $\kappa = 100$–200 for condition IV of Chang & Tarbell's results).

Another waveform studied in the curved tube is a pulsatile flow, which consists of both sinusoidally oscillating and steady components. Talbot & Gong (1983) investigated pulsatile flow by laser Doppler velocimetry, and the second set of conditions they used are similar to ours (i.e. $\delta = 1/7$, $\alpha = 12.5$, peak $\kappa = 372$, and mean $\kappa = 186$). They studied entrance flow, where the flow enters a curved portion with a nearly flat velocity profile and gradually develops downstream, but is not fully developed in the 180° curved tube. Therefore, we cannot compare our results with theirs in a detail; however, some features of intermittent and pulsatile flow are recognized. One remarkable result is the effect of the steady flow component. Our intermittent flow for $\alpha > 8$ shows that the axial velocity shifts towards the inside of the bend in an accelerating phase of a systole, and shifts towards the opposite side in a decelerating phase of a systole. On the other hand, except for the inlet section, the pulsatile flow studied by Talbot & Gong tends to shift to the outside of the bend during the entire period, similar to steady flow. This discrepancy means that the viscous force constantly prevails against the inertial force if a steady component of the same magnitude as the oscillating component is imposed. The effect of the steady component was more clearly indicated by Rindt *et al.* (1991). They numerically studied pulsatile flow in a 90° curved tube and examined the effect of the frequency for $\delta = 1/6$, $\alpha = 7.8$–24.7, peak $\kappa = 327$, and mean $\kappa = 204$. Their results show the secondary flow forms a constant Dean vortex even at high frequency (i.e. $\alpha = 24.7$), and they concluded that the secondary flow in a pulsatile flow is determined by the steady component.

The other remarkable difference between intermittent flow and pulsatile flow is the role of a diastole. In most of our cases, the flow in a diastole is dominated by the development of a boundary layer and by locally induced secondary flow. On the other hand, pulsatile flow is dominated by imposed transverse pressure gradients even in a diastole. Therefore, the magnitude of the velocity components oscillates as a function of the instantaneous flow rate, but the nature of the flow does not change between a

https://doi.org/10.1017/S0022112097006538 Published online by Cambridge University Press

systole and a diastole. The result is that for pulsatile flow, the flow profile in a systole is not sensitive to the flow profile in a diastole, while it is sensitive for intermittent flow.

4. Summary

From our simulations of the intermittent flow in strongly curved tubes during systolic and diastolic phases, we showed that the flow does not completely disappear during the diastolic period, and the residual secondary flow remains until the end of the diastolic phase. Therefore, the secondary flow is strongly affected by the nature of the residual vortex at the beginning of the systolic phase, so that the stationary diastolic period governs the generation of the secondary flow pattern. For $\eta = 0$ and $1/5$, an additional vortex occurred near the inner wall, while for $\eta = 1/3$ and $1/2$, additional vortices are not formed, but the secondary flow velocity increases locally. The intermittent flow in a curved tube is therefore shown to be strongly affected by the flow in the stationary diastolic period.

This study was partially supported by the Daiwa Research Institute Co., Ltd.; by a Grant-in-Aid for General Scientific Research from the Japanese Ministry of Education, Science, and Culture, Grant-in-Aid for Scientific Research on Priority Areas; and by the Scientific Research Promotion Fund in Japan. The authors highly appreciated the helpful suggestions about the numerical procedure given by Professor M. Akiyama in Utsunomiya University.

Appendix. Calculation of the secondary-flow stream function

In this study, development of the flow in the axial direction was assumed and the secondary-flow stream function was assumed to exist in the transverse direction.

The stream function, $\Psi_{A,B}$, physically corresponds to the bulk flow between two points, A and B, as

$$\Psi_{A,B} = \int_B^A \boldsymbol{u}\delta\boldsymbol{n}. \tag{A 1}$$

The secondary-flow streamlines shown in this study were drawn as contours of constant stream function, and the maximum of the stream function, Ψ_{max}, indicates the centre of the largest vortex.

The relationship between the stream function and the two velocity components in the transverse section is given as

$$u = -\frac{1}{rA}\frac{\partial}{\partial\phi}(\Psi), \qquad v = \frac{1}{A}\frac{\partial}{\partial r}(\Psi), \tag{A 2}$$

where the vorticity, Ω_θ, is written in terms of the stream function and the flow components as

$$\begin{aligned}\Omega_\theta &= \frac{1}{rA}\left[\frac{\partial}{\partial r}(rv) - \frac{\partial}{\partial\phi}(u)\right]A \\ &= \frac{1}{r}\left[\frac{\partial}{\partial r}\left(\frac{r}{A}\frac{\partial}{\partial r}(\Psi)\right) - \frac{\partial}{\partial\phi}\left(-\frac{1}{rA}\frac{\partial}{\partial\phi}(\Psi)\right)\right].\end{aligned} \tag{A 3}$$

Rewriting (A 3), an expression for calculating the stream function can be written

https://doi.org/10.1017/S0022112097006538 Published online by Cambridge University Press

as

$$\frac{\partial}{\partial r}\left[\frac{r}{A}\frac{\partial}{\partial r}(\Psi)\right]+\frac{\partial}{\partial \phi}\left[\frac{1}{rA}\frac{\partial}{\partial \phi}(\Psi)\right]=\frac{\partial}{\partial r}(rv)-\frac{\partial}{\partial \phi}(u). \tag{A 4}$$

Because the right-hand terms are determined from numerical calculations described in this paper, the stream function can be determined by numerically integrating (A 4).

REFERENCES

Berger, S. A. & Talbot, L. 1983 Flow in curved pipes. *Ann. Rev. Fluid Mech.* **15**, 461.

Chandran, K. B. 1993 Flow dynamics in the human aorta *J. Biomech. Engng* **115**, 611.

Chandran, K. B. & Yearwood, T. L. 1981 Experimental study of physiological pulsatile flow in a curved tube. *J. Fluid Mech* **111**, 59.

Chang, L.-J. & Tarbell, J. M. 1985 Numerical simulation of fully developed sinusoidal and pulsatile (physiological) flow in curved tubes. *J. Fluid Mech.* **161**, 175.

Chang, L.-J. & Tarbell, J. M. 1988 A numerical study of flow in curved tubes simulating coronary arteries. *J. Biomech.* **21**, 927.

Eckmann, D. M. & Grotberg, J. B. 1988 Oscillatory flow and mass transport in a curved tube. *J. Fluid Mech.* **188**, 509.

Gessener, F. B. 1973 Hemodynamic theories of atherogenesis. *Circ. Res.* **43**, 259.

Hamakiotes, C. C. & Berger, S. A. 1988 Fully developed pulsatile flow in a curved pipe. *J. Fluid Mech.* **195**, 23.

Hamakiotes, C. C. & Berger, S. A. 1990 Periodic flows through curved tubes: the effect of the frequency parameter. *J. Fluid Mech.* **210**, 353.

Konno, T. Satoh, Y. & Tanishita K. 1994 Secondary flow augmentation in the diastolic phase of physiologically intermittent flow in a curved tube. *VDI* **17**–107, 205.

Ku, D. N., Giddens, D. P., Zarins, C. K. & Glagov, S. 1985 Pulsatile flow and atherosclerosis in the human carotid bifurcation. *Arteriosclerosis* **5**, 293.

Lin, J. Y. & Tarbell, J. M. 1980 An experimental and numerical study of periodic flow in a curved tube. *J. Fluid Mech.* **100**, 628.

Lyne, W. H. 1971 Unsteady viscous flow in a curved pipe. *J. Fluid Mech.* **45**, 13.

Naruse, T., Nishina, Y., Kugenuma, S. & Tanishita, K. 1990*a* Developing oscillatory flow in a strongly curved tube. *JSME* **56**, 2562.

Naruse, T., Nishina, Y., Kugenuma, S. & Tanishita, K. 1990*b* Developing pulsatile flow in the aortic arch. *JSME* **56**, 3625.

Nerem, R. M. 1992 Vascular fluid mechanics, the arterial wall, and atherosclerosis *Trans. ASME, J. Biomech. Engng* **114**, 274.

Patankar, S. V. 1981 A calculation procedure for two-dimensional elliptic situations. *Num. Heat Transfer* **4**, 409.

Pedley, T. J. 1980 *The Mechanics of Large Blood Vessel*, p. 235. Cambridge University Press.

Rabadi, J. J., Simon, H. A. & Chow, J. C. F. 1980 Numerical solution for fully developed, laminar pulsating flow in curved tubes. *Num. Heat Transfer* **3**, 225.

Rindt, C. C. M., Steenhoven, A. A. van, Janssen, J. D. & Vossers, G. 1991 Unsteady entrance flow in a 90° curved tube. *J. Fluid Mech.* **226**, 445.

Smith, F. T. 1975 Pulsatile flow in curved pipes. *J. Fluid Mech.* **71**, 13.

Talbot, L. & Gong, K. O. 1983 Pulsatile entrance flow in a curved pipe. *J. Fluid Mech.* **127**, 1.

Weinbaum, S. & Parker, K. H. 1975 The laminar decay of suddenly blocked channel and pipe flows. *J. Fluid Mech.* **69**, 729.

Wesolowski, S. A., Fries, C. C., Sabini, A. M., & Sawyer, R. N. 1965 Significance of turbulence in hemic systems and in the distribution of the atherosclerotic lesion. *Surgery* **57**, 105.

Wilkinson, J. H. & Reinsh, C. 1971 *Linear Algebra.* Springer.

https://doi.org/10.1017/S0022112097006538 Published online by Cambridge University Press